Journal of Manufacturing Processes 118 (2024) 187–194

Contents lists available at ScienceDirect

Journal of Manufacturing Processes

journal homepage: www.elsevier.com/locate/manpro

Research article

NURBS-based path planning for aerosol jet printing of conformal electronics

Anushrut Jignasu, Jeremy D. Rurup, Ethan B. Secor, Adarsh Krishnamurthy *

Department of Mechanical Engineering, Iowa State University, Ames IA 50014, USA

ARTICLE INFO

Keywords:
Non-planar
Aerosol Jet Printing
NURBS
Conformal

ABSTRACT

Conformal printing offers a promising capability to integrate complex electronic functionality with intricate objects consisting of curved surfaces. However, motion planning to support these printing configurations presents a challenge, in part due to conventional reliance on tessellated surface representations that limit the accuracy and scalability of the printing process. In this paper, we introduce a direct approach to conformal aerosol jet printing on topographically complex surfaces, represented using non-uniform rational B-splines (NURBS). Using the NURBS surface definition directly offers a scalable and continuous approach for toolpath generation, which is well-aligned with standard computer-aided design practices. We select a patch that directly corresponds to the area of interest on the NURBS surface and extract the associated surface points. These surface points are then appropriately connected to generate the machine code (G-code) for a 3-axis printing system. We demonstrate this capability by printing a strain gauge on a curved model of a wind turbine blade. Our approach offers a promising avenue for manufacturing printed electronics with diverse applications that require conformal printing. This approach is particularly valuable for incorporating printed circuits on intricate underlying structures, including structural health monitoring for aerospace and civil infrastructure applications.

1. Introduction

Digital printing technologies fuel a broad trend toward increasing the integration of electronic components with structures. However, planar form factors remain dominant in practice due to simplicity in both the physical manufacturing process and digital process planning tools [1]. The planar nature limits the utility of printed electronics to planar parts, drastically reducing the scalability and robustness of the printing technology. In contrast, conformal printing methods involve depositing functional material onto non-flat, 3D surfaces, creating electronics that can conform to the contours of the object. Conformal printing can ultimately facilitate the concept of *functional objects*, particularly those with curved geometries. A variety of compelling applications of conformal patterning technologies exist [2], including in wireless communication [3], structural health monitoring [4], and bio-integrated electronics [5].

The research community continues to explore different conformal printing approaches. Contact printing methods, such as direct ink writing, pose challenges for conformal deposition due to their sensitivity to nozzle-surface distance and collision avoidance requirements. Among non-contact printing methods, aerosol jet printing (AJP) is a compelling technology due to its high standoff distance of 1–5 mm, high-resolution capability ($\approx 20\,\mu m$), and compatibility with electronically functional materials. In particular, the relatively larger standoff distance of AJP increases its tolerance to nozzle-substrate misalignment and surface roughness, giving it an edge over alternative patterning methods such as inkjet, electrohydrodynamic jet, and direct ink write printing. Its considerable standoff distance has especially gained AJP relevance in electronics packaging applications with 2.5D geometry [6,7]. A recent demonstration of AJP on additively manufactured drone components [8] shows a viable path away from more conventional 2D printed circuit boards, enabling multi-functional electro-mechanical devices and creating opportunities for lightweight designs.

The evolution of conformal AJP offers potential for novel applications but also introduces unique challenges regarding toolpath generation, substrate adherence at oblique angles, and material compatibility. Specifically, toolpath generation presents a major bottleneck in the process development and limits the utility of these methods that should, in principle, support rapid prototyping. Given the significant bottleneck in toolpath generation and the limitations of current planar printing methods, there is a pressing need for innovative approaches that can accommodate conformal AJP on non-planar 3D surfaces.

Ideally, a flexible printing framework should generate toolpaths for creating custom electronic circuits on a non-planar surface, given a computer-aided design (CAD) model of the underlying object. In CAD, boundary representations (B-reps) are the de facto standard for representing objects based on the boundary surfaces. The CAD software primarily utilizes parametric representations of curved surfaces, specifically non-uniform rational B-splines (NURBS), to define the boundary

* Corresponding author.
E-mail address: adarsh@iastate.edu (A. Krishnamurthy).

https://doi.org/10.1016/j.jmapro.2024.03.031
Received 15 December 2023; Received in revised form 21 February 2024; Accepted 11 March 2024
Available online 20 March 2024

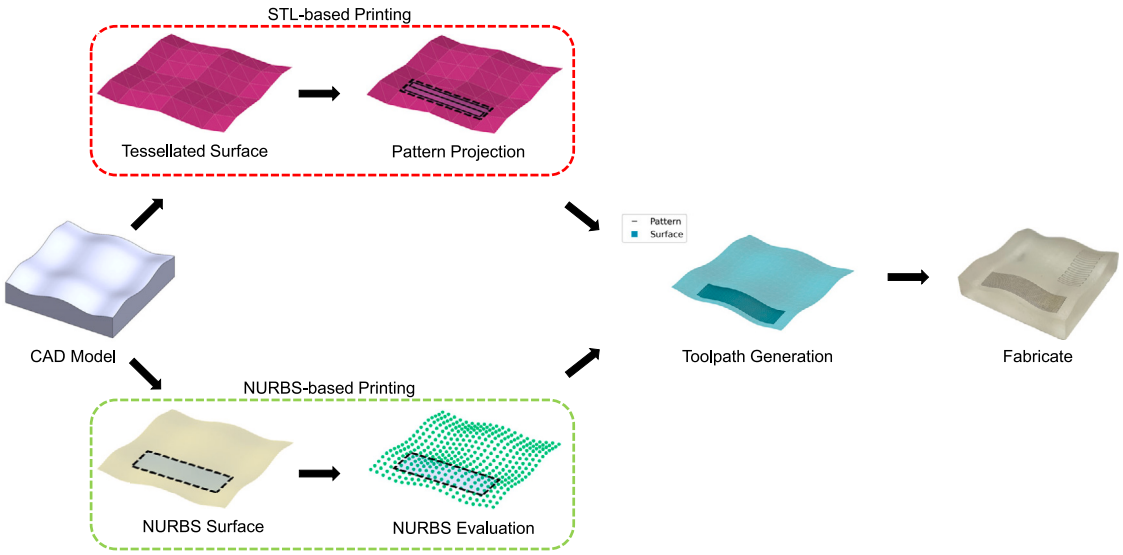

Fig. 1. Overview of our pipeline. We begin with a NURBS definition of a surface (highlighted by green box), allowing us to select a region of interest, as opposed to previous approaches that project a pattern on a tessellated representation (highlighted by red box). We evaluate the NURBS surface in this region of interest to generate toolpath points and subsequently use them for conformal ink deposition. (For interpretation of the references to color in this figure legend, the reader is referred to the web version of this article.)

Nomenclature

AJP	Aerosol Jet Printing
NURBS	Non-Uniform Rational B-Splines
G-code	Geometric Code
FDM	Fused Deposition Modeling
SLA	Stereolithography

surfaces. Traditionally, toolpath generation algorithms tessellate the NURBS surfaces to triangles. However, owing to truncation errors common during tessellation, there are inaccuracies associated with the tessellated representations of the objects [9–11]. These errors are usually extended to the toolpath generation process and often lead to incomplete toolpath information. In addition, specifically in AJP, this leads to inaccuracies in the standoff distance, reducing the quality of the printed circuits. In extreme cases, it can also lead to collisions between the print head and the base object, potentially damaging the manufacturing equipment.

In contrast, directly using the NURBS surfaces to generate the toolpath eliminates the truncation problem since they offer a level of control and accuracy that is unmatched by triangles. However, most slicing programs for toolpath generation utilize tessellated CAD models, owing in part to the relatively simpler plane-triangle intersection algorithms for traditional slicing and also in part due to the challenging nature of slicing parametric surfaces. However, previously, NURBS-based CAD models [12] have been directly sliced for layered manufacturing processes [13–15]. They have also been used for generating curved deposition layers for fused deposition modeling (FDM) printing [16,17]. Computing toolpaths on freeform surfaces is similar to the computation of fiber paths in composites, which has been investigated in previous studies [18,19]. Reference toolpaths can be found using a geodesic path, offset over the entire surface to determine parallel toolpaths [20]. Ravi Kumar et al. [21] investigated three different methods for computing geodesics on both parametric and tessellated surfaces, and showed that the most accurate method of computing geodesics is directly on the NURBS surface. Following the same concept, in this paper, we generate toolpaths for conformal printing directly using NURBS surfaces.

Traditional toolpath generation for extrusion 3D printing primarily involves planar motion because the printing is performed layer-by-layer. Most 3D printing toolpath generation algorithms first slice the 3D CAD model and extract the contours for each layer. The toolpaths are then generated for the contour and infill operation. However, the Z coordinate for each layer remains the same, and the print head is moved only along the XY plane within each layer. This leads to planar material deposition and often generates the commonly known staircase effect for curved geometries. For conformal AJP, the Z coordinate of the print head must vary in conjunction with movement in the XY plane to maintain the standoff distance, leading to conformal material deposition. In this work, by utilizing a NURBS definition of geometry, we can select regions of interest on a geometry of choice, selectively compute toolpaths for that region, and deposit a functional ink using AJP for the selected region without the staircase effect. Furthermore, owing to the NURBS parameterization, we have more local control over pattern placement on the underlying object.

We propose an end-to-end framework for conformal aerosol jet printing that uses a standard 3-axis printer. We use the NURBS definition of the underlying object to directly generate the toolpaths for conformal electronics. We then employ it to fabricate circuits on topographically complex surfaces. An overview of our approach is shown in Fig. 1. We begin with a NURBS definition derived from the CAD model for computing toolpaths as opposed to the conventional approach of projecting patterns onto tessellated representations of the CAD model. In essence, our contributions include:

- A conformal aerosol jet printing method directly utilizing the NURBS definition of CAD models for toolpath computation and generation.
- An approach to extract the NURBS sub-patch of a region of interest and generate circuit patterns on topographically complex surfaces.
- Application of conformal AJP framework to fabricate a functional strain gauge circuit on a model of a wind turbine blade using a 3-axis printer.

The rest of the paper is arranged as follows. In Section 2, we provide a basic background on NURBS and aerosol jet printing. In Section 3, we provide details of our approach for curved toolpath generation using NURBS surfaces. We demonstrate our approach on two different NURBS geometries in Section 4. We finally conclude and highlight possible future research directions in Section 5.

2. Background and related work

2.1. NURBS representation and toolpath generation

We use the NURBS definition to represent the geometry of the surface. In our approach, we use the NURBS definitions directly to generate the G-code for a toolpath inside a user-defined region of interest. NURBS are the most general version of splines used to parametrically represent curve surfaces. Formally, the position vector $\mathbf{S}(u, v)$ describing a point on the NURBS surface parameterized using (u, v) is defined as:

$$\mathbf{S}(u,v) = \frac{\sum_{i=0}^{n}\sum_{j=0}^{m} N_i^p(u) N_j^q(v) w_{ij} \mathbf{P}_{ij}}{\sum_{i=0}^{n}\sum_{j=0}^{m} N_i^p(u) N_j^q(v) w_{ij}}. \tag{1}$$

The basis functions of NURBS, N_i^p and N_j^q, are polynomials recursively computed using Cox-de Boor recursion formula in Eq. (2), where u is the parameter value and N_i^p is the ith basis function of degree p.

$$N_i^p(u) = \frac{u - u_i}{u_{i+p} - u_i} N_i^{p-1}(u) + \frac{u_{i+p+1} - u}{u_{i+p+1} - u_{i+1}} N_{i+1}^{p-1}(u) \tag{2}$$

$$N_i^0(u) = \begin{cases} 1 & \text{if } u_i \le u \le u_{i+1} \\ 0 & \text{otherwise} \end{cases} \tag{3}$$

Here, the knots (u_i) are the elements of the knot vector $\mathbf{U}$ (similarly, $v_i \in \mathbf{V}$). The knot vector is a non-decreasing sequence of parametric coordinates, which divides the B-spline into non-uniform piecewise functions. Intuitively, the knots determine the location of the control points in the parametric space. The basis functions N_i^p span the parametric domain based on the knot vector and degree as shown in Eqs. (2) and (3). Note that the formulation explained in Eq. (1) uses the vector notation, where $\mathbf{P}_{ij}$ is the control point embedded in $\Re^3$. Fig. 2 shows the mapping from the parametric space to the model space for a NURBS surface.

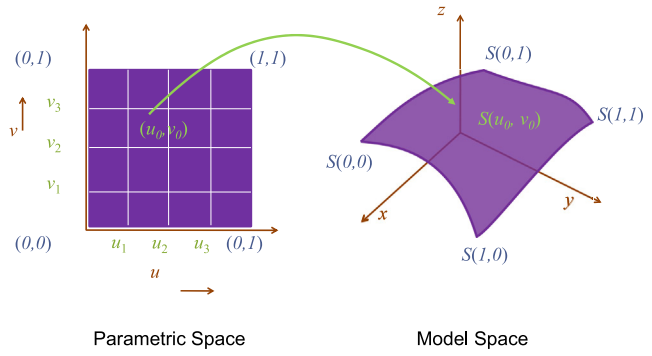

Fig. 2. NURBS definition in parametric and its mapping to model space.

Several researchers have previously explored slicing for G-code generation from NURBS representation. These include using ray-casting algorithm [22], converting NURBS to circular arcs and cubic Bézier curves [23], a box-plane intersection scheme [24] for contour generation, etc. The traditional triangle slicing approach cannot be directly adapted to our work as our geometry is defined using a parametric domain. As the end goal of the slicing operation is to identify points lying on the surface of the geometry, we directly utilize the NURBS surface definition to generate the points on the surface. In our framework, all operations are performed using the NURBS-Python library [25].

2.2. Aerosol jet printing

In aerosol jet printing, a functional ink is atomized to produce 1–5 μm droplets. A gas flow carries these droplets into a printhead, where a concentric sheath gas surrounds the aerosol stream and accelerates it through a deposition nozzle [26]. The high velocity (≈ 10–100 m/s) aerosol jet remains focused for 1–5 mm beyond the nozzle exit, enabling the high standoff distance and approximately line-of-sight patterning crucial for conformal printing. Feng [27] has documented the variability of standoff distances and its effects on the flow of the aerosol jet. Complex patterns can be fabricated additively by coupling the aerosol jet printhead with a digitally controlled motion system.

Despite AJP being a promising candidate for conformal deposition, even one-off demonstrations with idealized geometries (e.g., spheres and cylinders) require time-consuming fixture design, toolpath development, and alignment. Paulsen et al. [28] and Blumenthal et al. [29] were among the first to demonstrate the basic compatibility of AJP with a wide range of conformal electronics fabrication modalities, exploiting the high print offset, digital nature, and line-of-sight patterning of AJP. Gu et al. [30] followed with a more systematic and detailed approach to printing fillets for electrical interconnections between surfaces of different heights, a common challenge for microelectronics packaging. More recently, Vella et al. [31] and Gu et al. [32] provided thorough studies for printing functional electronics on well-defined 3D objects, including cylinders and cones. Saeidi-Javash et al. [33] and Zeng et al. [34] demonstrated quasi-3D conformal AJP of 2D nanomaterials using a 3-axis printer. Additionally, Rosker et al. [35] and Werum et al. [36] demonstrated AJP with 3D additively manufactured substrates. Such applications form the current state of the art that can enable increased complexity of both the mechanical substrate and the additively patterned electronic devices to create multifunctional structural devices. However, while these examples illustrate the promise of AJP for conformal electronics fabrication, they are constrained by traditional motion planning strategies and are inherently challenging to scale.

2.3. Strain gauges

In recent years, the study and application of strain sensors have garnered considerable attention, attributed to their inherent capability to detect and quantify geometric deformations in various materials. Such deformations, whether induced by external forces or intrinsic material properties, are indispensable for monitoring applications [37]. The fundamental operating principle of these sensors is the change in resistivity with strain. When subjected to deformation, there is an associated change in the sensor's resistance. This alteration in resistance subsequently leads to a variation in the voltage across the sensor. By monitoring this voltage differential, one can effectively infer the magnitude of strain imparted to the object.

Our proposed sensor design is predicated upon the principles of the Wheatstone bridge, specifically its quarter-bridge configuration. Within this configuration, the strain gauge acts as one of the arms of the bridge. Any deformation experienced by the gauge and the consequent change in its resistance disrupts the bridge's balance. This disruption manifests as a voltage difference across the bridge proportionally related to the strain the gauge has experienced. A prevalent design for these strain gauges is a serpentine configuration [38,39]. This design, characterized by its extended conductive pathway within a limited area, ensures detectable resistance changes even under minimal strain conditions. Importantly, the serpentine architecture ensures uniform strain distribution across the gauge, leading to reproducible and reliable measurements.

3. Conformal AJP framework

In this paper, we propose a new framework for conformal aerosol jet printing by directly using the NURBS representations for curved surfaces with a 3-axis aerosol jet printer. We first describe the conformal AJP process for depositing inks onto a curved surface in Section 3.1, followed by toolpath generation in Section 3.2. We also elaborate on bed alignment for fabrication in Section 3.3 and strain measurement in Section 3.4.

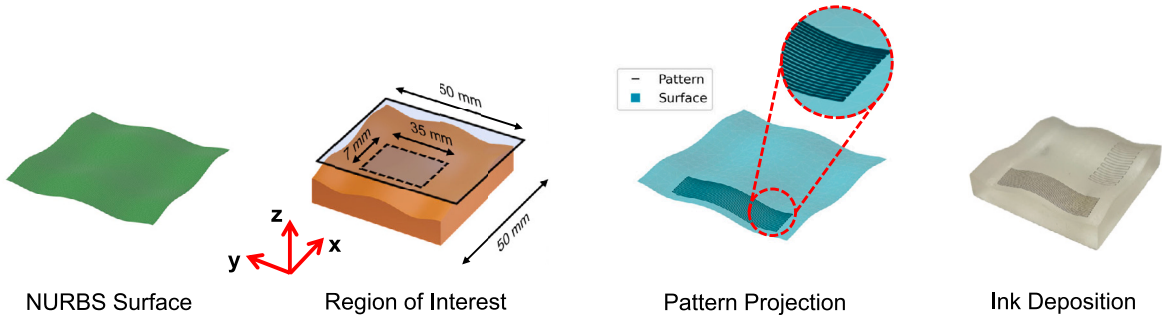

Fig. 3. Overview of our pipeline. We begin with a NURBS definition of a surface, allowing us to select a region of interest. We evaluate the NURBS surface in this region of interest to generate toolpath points and subsequently use them for conformal ink deposition.

3.1. Aerosol jet printing configuration

Liquid-phase printing methods are unique from many other additive technologies in that functional, solid material is transported and deposited on the surface via a functional ink. For our aerosol jet printer, in particular, a piezoelectric transducer is used to ultrasonically atomize aerosol droplets, which are transported to the printhead and ejected from the nozzle with a gas flow referred to as the carrier gas. A sheath gas is also introduced in the printhead, surrounding and focusing the aerosol-rich carrier gas flow. The flow rates of these gases are the most basic controls to adjust the deposition rate and trace width on an aerosol jet printer.

Printing was performed using a custom-built, 3-axis aerosol jet printer. The motion system comprises of three linear motion stages, allowing for Cartesian motion in the XYZ directions, and is controlled via a Galil DMC-4040 motion controller. Printing was performed with a print speed of 5 mm/s, a nozzle diameter of 200 μm, a cartridge temperature of 20 °C, and a substrate temperature of 20 °C. We set the aerosol and sheath gas flow rates to 12 and 60 sccm, respectively.

We do not consider the print speed as part of the toolpath planning algorithm and leave it as an individual parameter with a user-defined value. Print speed will generally affect both the printed line width and the total volume of deposited material for a pre-determined toolpath [40]. The ideal print speed is highly situational and dependent on ink properties and other process parameters. Our chosen print speed was determined empirically based on comprehensive testing with our specific ink and printer setup. With this print speed, there was minimal spreading of liquid ink on the substrate surface, and the printed traces remained electrically continuous.

For all printing, the nozzle-substrate standoff distance was set to 2 mm, well within the limits recommended by Feng [27]. The deposition physics may differ for a surface-oblique orientation imposed by 3D geometry. However, the recommended 1–5 mm standoff was anticipated to be largely valid and result in high-quality printed lines. The substrate was fabricated via SLA on a Formlabs Form2 printer with general-purpose clear resin or, where specified, high-temperature resin.

We use two different silver nanoparticle functional inks. First, a commercial ink was obtained from UT Dots, Inc, called UTD-Ag40X, a dispersion of 40% w/v silver nanoparticles in xylenes. This was mixed with xylenes and terpineol in a ratio of 2:7:1 v/v UTD-Ag40X, xylenes, and terpineol. The second ink was EI-615, obtained from Electroninks.

3.2. Toolpath generation

Toolpath generation is based on utilizing the NURBS surface definition. We select a region of interest (ROI) on the NURBS surface (shown in Fig. 3). The placement of this region of interest is user-specific and application-specific. Given that we are selecting a sub-area of the original surface, the area-specific surface points can be derived by selecting a subset of parametric *uv* coordinates. This is achieved by identifying the parametric span of the ROI.

The parametric span can be considered as a portion of the NURBS surface. The actual shape of this portion is dependent on the selected set of *uv* values. For this span of parametric (*uv*) coordinates, we evaluate the NURBS surface to generate the corresponding surface points. Each surface point has X, Y, and Z coordinates, which we use for G-code generation. AJP is a non-contact additive manufacturing process, and all the surface points of the patch are offset by a standoff distance of 1–5 mm between the nozzle and the substrate. AJP is relatively tolerant to variations in this surface offset distance [27], but substantial variations outside this range can negatively affect aerosol impaction on the surface and, hence, line resolution. The toolpath is generated by connecting these surface points along a serpentine pattern.

After generating the points in the region of interest, the next step is to generate toolpaths interpretable by the 3-axis machine. During the G-code generation process, we add commands specifically for AJP functionality. The most notable of these are the commands for feed rates and a shutter mechanism, which allows us to selectively turn the aerosol flow on and off. Our specific machine natively accepts the Galil DMC language, although G-code is a universal intermediary.

3.3. Print bed alignment

Aligning the print bed coordinate system with the NURBS coordinate system is essential since any misalignment can lead to irregular pattern deposition, aerosol deposition outside the region of interest, potential nozzle-substrate collision, and damage to the printer. An example of substrate placement can be seen in Fig. 4. We define the *zero point* as the origin and select the bottom left corner of the print bed as the origin. The placement of the substrate as well as print head movements are with respect to this *zero point* in the XY plane. In the Z direction, the working distance is initially set by touching off and zeroing the nozzle to the print bed, establishing a nozzle-substrate distance of 2 mm.

Our printer's Z-axis resolution of 1.25 μm exceeds the practical requirements for AJP. A working distance of 1–5 mm is acceptable, with minor variations in this range having negligible impact on line quality and deposition rate. This tolerance allows for slight Z-height adjustments without requiring continuous recalibration, thus streamlining the printing process. Furthermore, we determine the correct Z height from the toolpath generation process at any given instance. These Z height values are automatically offset by the configured working distance during printing. No further printer calibration is required beyond this setup.

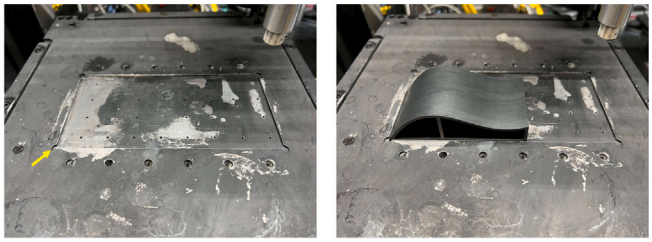

Fig. 4. Print bed with zero point (shown by yellow arrow, left) and the substrate aligned with the print bed. (For interpretation of the references to color in this figure legend, the reader is referred to the web version of this article.)

Table 1
Configuration parameters for the serpentine pattern on the NURBS surface shown in Fig. 3. We utilize these *uv* values for defining the region of interest of our serpentine pattern and evaluate the surface at all intermediate values, including u_{start} and u_{end}. We also give approximate dimensions of the fabricated patterns.

Metric	Pattern A	Pattern B
u_{start}, u_{end}	0.05, 0.2	0.4, 0.9
v_{start}, v_{end}	0.1, 0.8	0.1, 0.3
Width (mm)	~ 35	~ 10
Height (mm)	~ 7	~ 25

3.4. Strain measurement

To showcase the applicability of our method, we propose to use the deposited functional ink to measure the strain experienced by the substrate. To generate the strain sensor pattern, we make use of the same approach described in Section 3.2. However, given the intricate design of a strain sensor, we select multiple regions of interest to generate the final pattern. These regions correspond to the main sensor pattern, two individual electrodes and the circuitry joining the electrodes to the main sensor pattern. When generating toolpaths for fabrication, a combination of the surface points corresponding to the multiple regions of the sensor is considered. Once printed, wires were connected to the strain sensor and plugged into a breadboard, along with the static resistors comprising the remainder of the Wheatstone bridge. With the circuit completed and power supplied across the Wheatstone bridge, the substrate was manually deflected, placing the strain sensor in both tension and compression. The resulting changes in voltage were measured over time using a Keithley 2450 SourceMeter.

4. Results

We demonstrate our conformal AJP technique for multiple circuit patterns, leveraging the NURBS representation. An example deposition surface is shown in Fig. 5(a). We also import the NURBS surface into SolidWorks [41] and extrude along its depth to generate a volume (shown in Fig. 5(b)) that serves as a test substrate. We save this substrate geometry as an STL file and print using traditional SLA printing. This printed surface serves as our substrate for conformal printing.

We define two parametric spans in the *uv* space for defining two separate regions of interest. We select the surface evaluation delta (the step size used for sampling points in the parametric space) to be 0.05 and obtain 400 surface points within each region of interest. Two sets of patterns were fabricated onto the substrate (Fig. 5(b)) using the UTD-Ag40X silver nanoparticle ink. These patterns along with intra-pattern dimensions can be seen in Fig. 7. The configuration parameters for these patterns are shown in Table 1. Furthermore, we maintain a constant standoff distance from the substrate; we are always within a tolerance of 1–5 mm (the most commonly used offset distance for AJP), thus keeping the width of deposition constant.

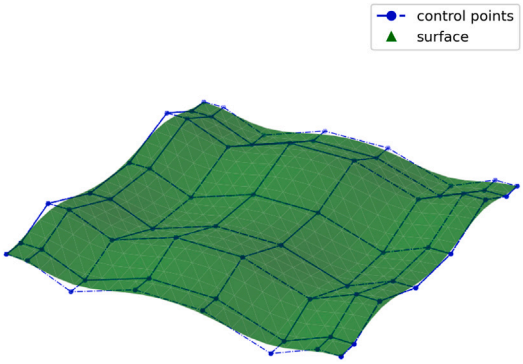

(a) *NURBS surface generated using the NURBS-Python library. We use a 3rd degree curve along the parametric u and v directions. We use an evaluation delta of 0.05.*

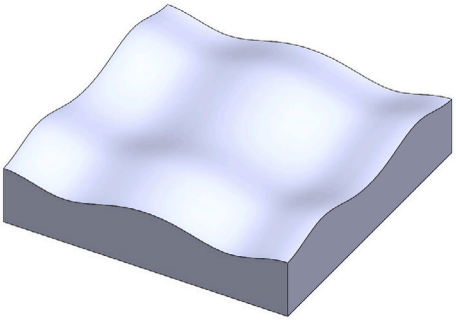

(b) *Volume generated using the NURBS surface (shown above) used to fabricate the substrate using SLA. We utilize a clear resin for fabrication.*

Fig. 5. Visualization of our (a) NURBS surface and (b) substrate on which we fabricate conformal patterns using Aerosol Jet Printing.

Table 2
Configuration parameters for the strain-sensor pattern on the wind turbine blade shown in Fig. 6. Region B in Fig. 8 is repeated twice and we refer to these repetitions as B_1 and B_2. They are equal in dimensions.

Metric	Region A	Region B_1	Region B_2
u_{start}, u_{end}	0.39, 0.64	0.64, 0.73	0.3, 0.39
v_{start}, v_{end}	0.11, 0.22	0.22, 0.31	0.22, 0.31
Width (mm)	~ 10	~ 6	~ 6
Height (mm)	~ 5	~ 1	~ 1

To demonstrate our method's real-world applicability, we print a model of a NACA-4418 wind turbine blade (shown in Fig. 6) and generate a conformal strain-sensor pattern on its top surface using Electroninks EI-615 silver ink. The wind turbine blade's geometry is also made up of two different curves along *u* and *v*. We again select the evaluation delta to be 0.05 and generate 400 surface points for each region of interest. We make 5 passes for the strain gauge pattern on the wind turbine blade to ensure electrical continuity on the rough substrate. To make the silver ink conductive, we sintered it at 100 °C for 1 h. The knot span selection for the main sensor is such that the dimensions are approximately 5 mm high and 10 mm wide. We showcase the pattern along with intra-pattern dimensions in Fig. 8. The distance between any two consecutive lines of the main pattern is approximately 250 μm. We make use of Formlabs' high temperature resin [42] to manufacture the wind turbine blade using SLA. The relative placement for the strain-sensor pattern is selected to be in a high curvature area, for the purpose of showing the robustness of our approach (see Table 2).

Close-up images of the conformal patterns show consistent aerosol deposition and uniform width of printed traces on both the NURBS surface and the wind turbine in Figs. 7 and 8, respectively. The resulting

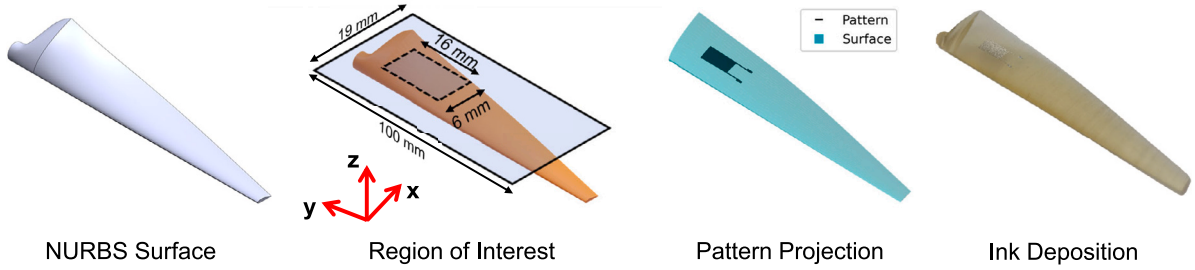

Fig. 6. Overview of our pipeline for conformal AJP on a wind turbine blade. We begin with a NURBS definition of the wind turbine blade, allowing us to select a region of interest. We evaluate the NURBS surface in this region of interest to generate toolpath points and subsequently use them for conformal ink deposition.

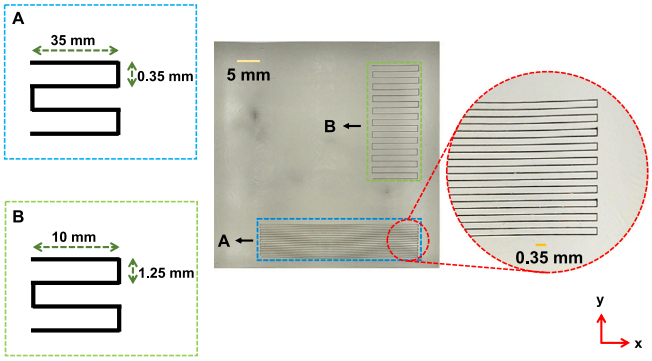

Fig. 7. Serpentine patterns for the NURBS surface are shown by two regions — region A and region B respectively. Region A is highlighted by the light blue box. Region B is highlighted by the orange box. The intra-pattern dimensions are shown in the highlighted boxes on the left. A closeup of region A is shown on the right. (For interpretation of the references to color in this figure legend, the reader is referred to the web version of this article.)

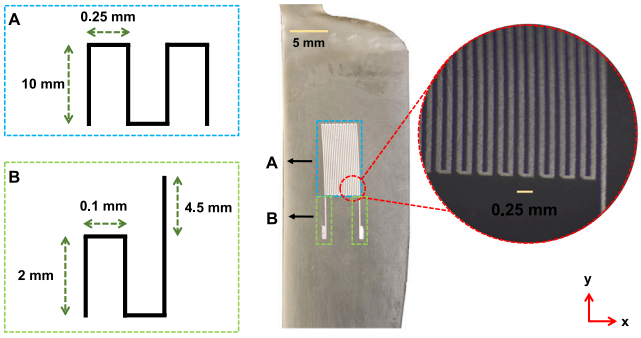

Fig. 8. Serpentine pattern for the wind turbine blade is split into two regions — region A and region B respectively. Region A is highlighted by the light blue box. Region B is repeated twice and is highlighted by the orange boxes. The intra-pattern dimensions are shown in the highlighted boxes on the left. A closeup of region A is shown on the right, including the transition between the regions. (For interpretation of the references to color in this figure legend, the reader is referred to the web version of this article.)

examples in this section showcase the viability of this methodology for motion planning to support conformal electronics fabrication on complex curved surfaces. In our methods demonstrated here, we do not explicitly control the length of each line of the serpentine pattern but rather the expanse of the region of interest in the parametric domain. We select multiple regions of interest for the strain sensor pattern on a model wind turbine blade to generate the final strain-sensor pattern, as shown in Fig. 8. The surface evaluation points from each of these regions are combined and subsequently used for toolpath generation and fabrication.

Table 3
Quantitative comparison between a coarse STL model and a NURBS model.

Model	Height (mm)	Chamfer distance (mm)
NURBS Surface	11.5	0.13
Wind Turbine Blade	12.7	0.21

The orientation of the substrate has limited impact on the print quality, provided the substrate's slope is not excessively steep. The thickness of the substrate does not affect the toolpath generation since we zero the nozzle to the bottom left corner of the print bed before every print. To better illustrate our method's capability in handling challenging geometries for aerosol deposition, we plot color maps of surface orientation for our test surfaces in Figs. 9(a) and 9(b). The color scale indicates the angle the surface normal vector makes at each point with respect to the build direction, with the build direction along the z-axis corresponding to the aerosol jet nozzle orientation. The change in angle depicts the nonplanar nature of the underlying geometry. Because the angle remains modest within the regions of interest (i.e., <30°), a fixed tilt configuration for the nozzle is able to maintain relatively uniform aerosol deposition for the patterns.

Furthermore, we showcase the effect of the surface approximation error by comparing a coarse tessellation STL model against the NURBS model. The basis for this example is to demonstrate that we can obtain higher accuracy with a NURBS surface definition. To generate deviation metrics, we utilize CloudCompare's [43] cloud-to-mesh distance measure to generate the color plots in Figs. 10(a) and 10(b). Areas with higher curvature are observed to have a relatively higher deviation than areas with lower curvature. Furthermore, as a quantitative measure of the error between a coarse STL and a NURBS model, we make use of the one-sided Chamfer distance ($\mathcal{L}_{CD}$) metric to measure the deviation of the STL model from the NURBS surface (Eq. (4)). It is defined as the average of the distances between each point $\mathbf{P_i}$ in point set $\mathbf{P}$ and its nearest neighbor in point set $\mathbf{Q}$.

$$\mathcal{L}_{CD} = \sum_{\mathbf{P_i} \in \mathbf{P}} \min_{\mathbf{Q_j} \in \mathbf{Q}} \|\mathbf{P_i} - \mathbf{Q_j}\|_2 \tag{4}$$

As can be seen in Table 3, the chamfer distance for the NURBS surface is about 0.13 mm, and for the wind turbine blade, it is 0.21 mm. Their values are almost 1% and 2% of the model heights, respectively.

To measure the strain variation, we consider the strain gauge to be one of the elements in a Wheatstone bridge. When a strain (compressive/tensile) is applied, the resistance changes, which unbalances the Wheatstone bridge and induces a measurable change in voltage. The magnitude and direction denote whether the input strain is compressive or tensile. We showcase our setup for measuring a change in voltage in Fig. 11 and a plot of corresponding output in Fig. 12. The observed data

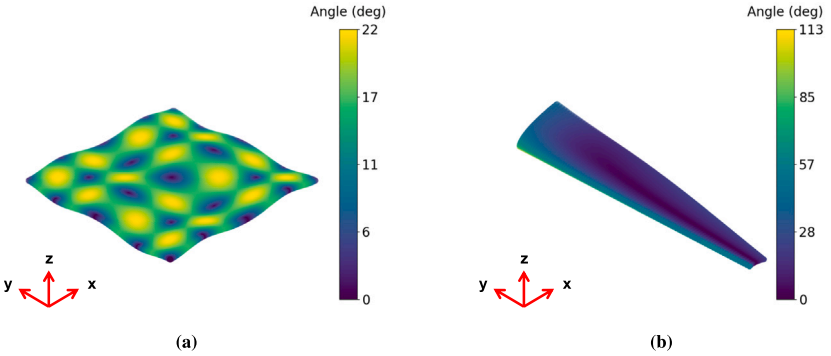

Fig. 9. Color maps of the angles the normal vectors make with the build direction for (a) the NURBS surface and (b) the wind turbine blade. The build direction is chosen to be along the Z axis. Areas with a higher curvature showcase a larger deviation in angles than areas with lower curvature.

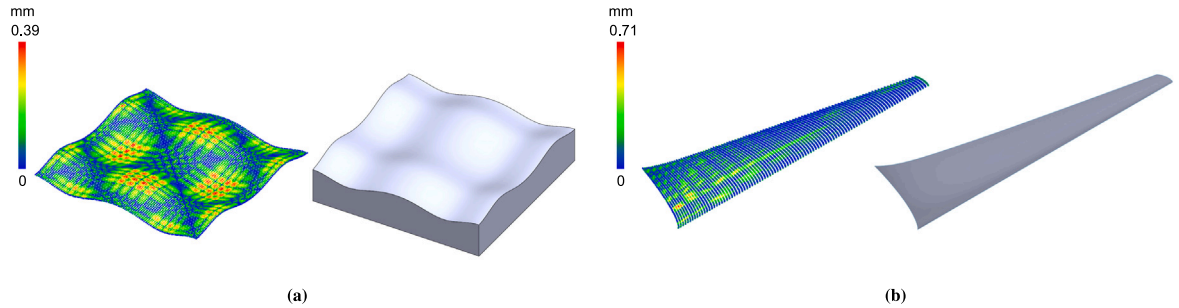

Fig. 10. The deviation of a coarsely tessellated model from the NURBS model (left). For reference, the STL is shown on the right. Areas with higher curvature have a relatively higher deviation.

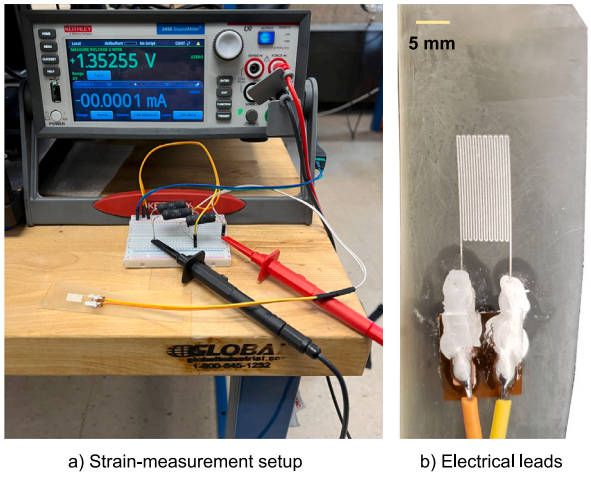

Fig. 11. Our strain measurement setup is shown in (a). We utilize a Keithley 2450 SourceMeter along with a custom breadboard setup with static resistors. We also show a close up of the attached electrical leads in (b).

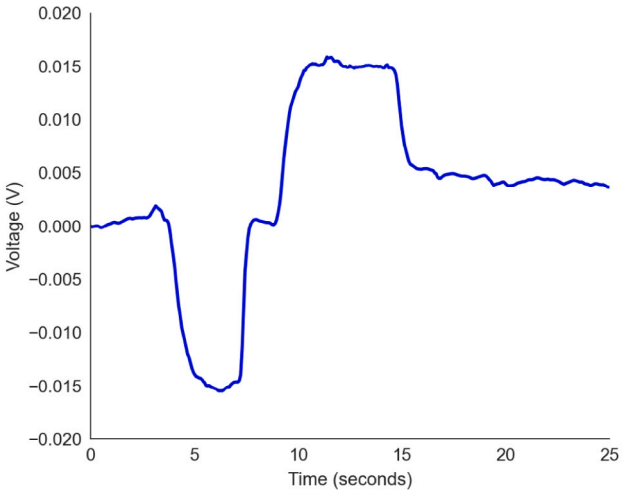

Fig. 12. Strain variation for the wind turbine blade as seen through a voltage difference over a period of time and measured using the setup shown in Fig. 11. Negative and positive voltage measurements between [4,7] second interval and [8, 15] second interval, suggest compressive and tensile strains respectively.

exhibits a dynamic response, highlighting the rapid adaptability of the strain gauge to sudden changes in load. We note compressive strain in the [4,7] second interval and tensile strain in the [8, 15] second interval.

5. Conclusions and future work

In this paper, we introduce a novel framework for conformal aerosol jet printing using a standard 3-axis printer to fabricate circuit patterns on complex geometries. We utilize NURBS definitions to define regions of interest on a geometry, design curved toolpaths specific to these regions, and showcase our method's applicability by manufacturing a strain gauge pattern on a model NACA standard wind turbine blade. In case the CAD geometry does not exist, an alternative approach would be to capture a point cloud of the substrate and then fit a NURBS surface to that point cloud. We can then use our framework to perform conformal printing.

Many traditional additive manufacturing methods, such as contact-printing methods like FDM and direct ink writing, rely on tessellated surface representations that impede their accuracy and scalability. Non-contact deposition provides advantages to overcome these challenges, but patterning methods, including inkjet and electrohydrodynamic jet

printing, are susceptible to nozzle-substrate misalignment and surface roughness. The fundamental tolerance of AJP to a wide range of standoff heights and even oblique jet orientation is a critical benefit that alters the constraints for suitable toolpath generation. Leveraging the scalability and accuracy of NURBS representations for curved 3D geometries, we have demonstrated a viable strategy for motion planning to support conformal electronics. Furthermore, extending this framework to 5-axis printing is technically feasible, as extracting surface normal orientation is straightforward from the NURBS definition. Future exploration and continued development hold the potential to establish a holistic approach for conformal electronics printing with expansive applications.

Declaration of competing interest

The authors declare that they have no known competing financial interests or personal relationships that could have appeared to influence the work reported in this paper.

Acknowledgments

This work was supported by the National Science Foundation, United States under grant number CMMI-2224303.

References

[1] Hines D, Gu Y, Martin A, Li P, Fleischer J, Clough-Paez A, et al. Considerations of aerosol-jet printing for the fabrication of printed hybrid electronic circuits. Addit Manuf 2021;47:102325.
[2] Rich SI, Jiang Z, Fukuda K, Someya T. Well-rounded devices: the fabrication of electronics on curved surfaces – A review. Mater Horiz 2021;8(7):1926–58. http://dx.doi.org/10.1039/D1MH00143D.
[3] Jun SY, Elibiary A, Sanz-Izquierdo B, Winchester L, Bird D, McCleland A. 3-d printing of conformal antennas for diversity wrist worn applications. IEEE Trans Compon, Packag Manuf Technol 2018;8(12):2227–35.
[4] Zymelka D, Togashi K, Ohigashi R, Yamashita T, Takamatsu S, Itoh T, et al. Printed strain sensor array for application to structural health monitoring. Smart Mater Struct 2017;26(10):105040.
[5] Herbert R, Lim H-R, Yeo W-H. Printed, soft, nanostructured strain sensors for monitoring of structural health and human physiology. ACS Appl Mater Interfaces 2020;12(22):25020–30.
[6] Stoukatch S, Laurent P, Dricot S, Axisa F, Seronveaux L, Vandormael D, et al. Evaluation of aerosol jet printing (AJP) technology for electronic packaging and interconnect technique. In: 2012 4th electronic system-integration technology conference. Amsterdam, Netherlands: IEEE; 2012, p. 1–5. http://dx.doi.org/10.1109/ESTC.2012.6542067, URL http://ieeexplore.ieee.org/document/6542067/.
[7] Seifert T, Baum M, Roscher F, Wiemer M, Gessner T. Aerosol jet printing of nano particle based electrical chip interconnects. Mater Today: Proc 2015;2(8):4262–71. http://dx.doi.org/10.1016/j.matpr.2015.09.012, URL https://linkinghub.elsevier.com/retrieve/pii/S2214785315007968.
[8] Goh GL, Dikshit V, Koneru R, Peh ZK, Lu W, Goh GD, et al. Fabrication of design-optimized multifunctional safety cage with conformal circuits for drone using hybrid 3D printing technology. Int J Adv Manuf Technol 2022;120(3–4):2573–86. http://dx.doi.org/10.1007/s00170-022-08831-y, URL https://link.springer.com/10.1007/s00170-022-08831-y.
[9] Cao W, Miyamoto Y. Direct slicing from autocad solid models for rapid prototyping. Int J Adv Manuf Technol 2003;21:739–42.
[10] Jamieson R, Hacker H. Direct slicing of CAD models for rapid prototyping. Rapid Prototyp J 1995;1(2):4–12.
[11] Kumar V, Dutta D. An assessment of data formats for layered manufacturing. Adv Eng Softw 1997;28(3):151–64.
[12] Requicha AAG, Rossignac JR. Solid modeling and beyond. IEEE Comput. Graph. Appl. 1992;12(5):31–44.
[13] Vuyyuru P, Kirschman C, Fadel G, Bagchi A, Jara-Almonte C. A NURBS-based approach for rapid product realization. In: Proceedings of the 5th international conference on rapid prototyping, the university of dayton. 1994, p. 229–39.
[14] Sikder S, Barari A, Kishawy H. Global adaptive slicing of NURBS based sculptured surface for minimum texture error in rapid prototyping. Rapid Prototyp J 2015.
[15] Ma W, But W-C, He P. NURBS-based adaptive slicing for efficient rapid prototyping. Comput Aided Des 2004;36(13):1309–25.
[16] Chakraborty D, Reddy BA, Choudhury AR. Extruder path generation for curved layer fused deposition modeling. Comput Aided Des 2008;40(2):235–43.
[17] Etienne J, Ray N, Panozzo D, Hornus S, Wang CC, Martínez J, et al. Curvislicer: Slightly curved slicing for 3-axis printers. ACM Trans Graph 2019;38(4):1–11.
[18] Nagendra S, Kodiyalam S, Davis J, Parthasarathy V. Optimization of tow fiber paths for composite design. In: 36th structures, structural dynamics and materials conference. American Institute of Aeronautics and Astronautics; 1995, p. 1031–41. http://dx.doi.org/10.2514/6.1995-1275.
[19] Setoodeh S, Blom A, Abdalla M, Gürdal Z. Generating curvilinear fiber paths from lamination parameters distribution. In: Structures, structural dynamics, and materials conference. American Institute of Aeronautics and Astronautics; 2006, p. 1875. http://dx.doi.org/10.2514/6.2006-1875.
[20] Scheirer N, Holland S, Krishnamurthy A. Fiber layup generation on curved composite structures. Comput Aided Des 2021;136:103031.
[21] Ravi Kumar G, Srinivasan P, Devaraja Holla V, Shastry K, Prakash B. Geodesic curve computations on surfaces. Comput Aided Geom Design 2003;20(2):119–33.
[22] Starly B, Lau A, Sun W, Lau W, Bradbury T. Direct slicing of STEP based NURBS models for layered manufacturing. Comput Aided Des 2005;37(4):387–97.
[23] Chacón JM, Sánchez-Reyes J, Vallejo J, Núñez PJ. G-code generation in a NURBS workflow for precise additive manufacturing. Rapid Prototyp J 2022;28(11):65–76.
[24] Gohari H, Barari A, Kishawy H. An efficient methodology for slicing NURBS surfaces using multi-step methods. Int J Adv Manuf Technol 2018;95:3111–25.
[25] Bingol OR, Krishnamurthy A. NURBS-python: An open-source object-oriented NURBS modeling framework in python. SoftwareX 2019;9:85–94. http://dx.doi.org/10.1016/j.softx.2018.12.005.
[26] Secor EB. Principles of aerosol jet printing. Flex Printed Electron 2018;3(3):035002. http://dx.doi.org/10.1088/2058-8585/aace28.
[27] Feng JQ. Mist flow visualization for round jets in aerosol jet® printing. Aerosol Sci Technol 2019;53(1):45–52.
[28] Paulsen JA, Renn M, Christenson K, Plourde R. Printing conformal electronics on 3D structures with aerosol jet technology. In: 2012 future of instrumentation international workshop (FIIW) proceedings. 2012, p. 1–4. http://dx.doi.org/10.1109/FIIW.2012.6378343.
[29] Blumenthal T, Fratello V, Nino G, Ritala K. Conformal printing of sensors on 3D and flexible surfaces using aerosol jet deposition. In: Nanosensors, biosensors, and info-tech sensors and systems, vol. 8691, International Society for Optics and Photonics; 2013, p. 86910P. http://dx.doi.org/10.1117/12.2009278.
[30] Gu Y, Hines DR, Yun V, Antoniak M, Das S. Aerosol-jet printed fillets for well-formed electrical connections between different leveled surfaces. Adv Mater Technol 2017;2(11):1700178.
[31] Vella S, Smithson CS, Halfyard K, Shen E, Chrétien M. Integrated capacitive sensor devices aerosol jet printed on 3D objects. Flex Printed Electron 2019;4(4):045005. http://dx.doi.org/10.1088/2058-8585/ab59c0.
[32] Gu Y, Park D, Bowen D, Das S, Hines DR. Direct-write printed, solid-core solenoid inductors with commercially relevant inductances. Adv Mater Technol 2019;4(1):1800312.
[33] Saeidi-Javash M, Kuang W, Dun C, Zhang Y. 3D conformal printing and photonic sintering of high-performance flexible thermoelectric films using 2D nanoplates. Adv Funct Mater 2019;29(35):1901930.
[34] Zeng M, Kuang W, Khan I, Huang D, Du Y, Saeidi-Javash M, et al. Colloidal nanosurfactants for 3D conformal printing of 2D Van der Waals materials. Adv Mater 2020;32(39):2003081. http://dx.doi.org/10.1002/adma.202003081.
[35] Rosker ES, Barako MT, Nguyen E, Radisic V, Goorsky MS, Tice J. Fully 3D printed high performance band-stop filters enabled by three-dimensional design. Flex Printed Electron 2022;7(3):035006. http://dx.doi.org/10.1088/2058-8585/ac825a, URL https://iopscience.iop.org/article/10.1088/2058-8585/ac825a.
[36] Werum K, Mueller E, Keck J, Jaeger J, Horter T, Glaeser K, et al. Aerosol jet printing and interconnection technologies on additive manufactured substrates. J Manuf Mater Process 2022;6(5):119. http://dx.doi.org/10.3390/jmmp6050119, URL https://www.mdpi.com/2504-4494/6/5/119.
[37] Lee G-Y, Kim M-S, Yoon H-S, Yang J, Ihn J-B, Ahn S-H. Direct printing of strain sensors via nanoparticle printer for the applications to composite structural health monitoring. Procedia CIRP 2017;66:238–42.
[38] Borghetti M, Serpelloni M, Sardini E. Printed strain gauge on 3D and low-melting point plastic surface by aerosol jet printing and photonic curing. Sensors 2019;19(19):4220.
[39] Agarwala S, Goh GL, Yeong WY. Aerosol jet printed strain sensor: Simulation studies analyzing the effect of dimension and design on performance (september 2018). IEEE Access 2018;6:63080–6.
[40] Tafoya RR, Secor EB. Understanding effects of printhead geometry in aerosol jet printing. Flex Printed Electron 2020;5(3):035004. http://dx.doi.org/10.1088/2058-8585/aba2bb, URL https://iopscience.iop.org/article/10.1088/2058-8585/aba2bb.
[41] SolidWorks Corp. SolidWorks. 2021 Education Edition. 2021, URL www.solidworks.com.
[42] Formlabs. Formlabs. 2023, URL www.formlabs.com.
[43] CloudCompare. CloudCompare (version 2.11.3). 2024, URL http://www.cloudcompare.org/.